Forward modeling of the coronal response to reconnection in an X-ray bright point

CHARLES KANKELBORG AND DANA LONGCOPE
Montana State University, Bozeman, MT 59717

Abstract

We present a novel gasdynamic model of the corona and transition region confined by a static flux tube. Our model allows completely general specification of an asymmetric flux tube geometry, so that detailed comparison with observations can be made. Nonlocal effects such as opacity and ambipolar diffusion are important to the transition region; it is shown that these effects can be modeled locally by straightforward modification of the radiative loss and thermal conduction terms. To illustrate the utility of a forward modeling approach, we use MDI magnetic field observations and the theory of reconnection through a separator to constrain a simulation of an X-ray bright point observed by TRACE. A straightforward comparison of measured light curves versus those generated by the simulation shows that the reconnection model is unable to account for the observations.

I. INTRODUCTION

The solar corona in regions of closed magnetic field is confined to loop structures, the geometry of the loops being defined by the magnetic field. The ends of these loops must connect to plasma at chromospheric temperatures, implying the existence of a transition region. Because magnetic flux is frozen in to the plasma, cross-section must vary inversely with the magnetic field strength. Moreover, the concentration of photospheric flux in kilogauss bundles must lead to a magnetic canopy structure (Gabriel 1976). Thus loop cross-sections are expected to vary in the corona, and even more so in the transition region. The corona, transition region, and magnetic field are therefore inextricably related. With few exceptions, however, models of coronal loops, the solar transition region and the magnetic field have evolved separately.

Scaling laws and static solutions of the energy balance equation for coronal loops were first descibed by Rosner, Tucker and Vaiana (1978, hereafter RTV). These models assumed constant cross-section, local thermodynamic equilibrium (LTE) and zero opacity even at chomospheric temperatures. The effect of varying cross-section on static coronal loop solutions was investigated numerically by Vesecky, Antiochos & Underwood (1979), for the special case of symmetry about the loop apex. Analytic solutions for coronal funnels were derived by Rabin (1991).

The above models treat the transition region superficially, as an extension of the optically thin corona with local ionization balance. McClymont & Canfield (1983) showed that optical depth in the lower transition region is an important factor in determining the stability of loops. The time-dependent loop model of Klimchuk, Antiochos and Mariska (1987) used a T^3 radiative loss dependence, prescribed by McClymont & Canfield, for the transition region. Peres *et al.* 1982 included a transition region modeled after the transition region equilibria of Vernazza, Avrett & Loeser (1981, hereafter VAL). Their implementation consisted of a modified radiative loss function with fine tuning of the heating function $E_H(T)$ to reproduce the chromospheric temperature profile of one of the VAL models. All of the gasdynamic models mentioned so far assume constant cross-section and symmetry about the loop apex.

Since the publication of the VAL transition region models, significant advancements have been made by Fontenla, Avrett & Loeser (1990, hereafter FAL). The FAL models demonstrate the importance of ambipolar diffusion, which smooths the ionization gradient, alters the plasma emissivity, and augments thermal conduction. The literature to date records no influence of these results on loop modeling.

Nearly all of the loop models published to date use a coronal radiative loss model similar to the original one tabulated by RTV. However, recent results on coronal abundances (reviewed by Feldman, 1992) imply that the ions responsible for most of the coronal radiation are enhanced in the closed corona by a factor of ~4 over photospheric abundances.

The model described in this paper is a novel synthesis of realistic magnetic field geometry, gasdynamic coronal loop modeling, recent advances in transition region modeling, and improved estimates of the coronal radiative loss. Specifically, our model incorporates the following features:

- Configurable, asymmetric 3D flux tube geometry, including variations in cross-sectional area and gravitational acceleration from the upper chromosphere (10^4 K) to the corona (> 10^6 K).
- Enhanced thermal conduction due to ambipolar diffusion.
- Corrections to the transition region radiative loss due to optical depth and non-LTE ionization balance.
- Enhanced coronal radiative losses due to the FIP effect.

These refinements enable modeling of observed solar loops with significantly improved realism. Inputs from all types of observations, from photospheric magnetograms to soft x-ray images, may be used in meaningful ways to constrain this model. As a result, the detailed predictions of heating theories may be tested quantitatively by forward modeling of their effect on observed loops.

In this paper, we describe the loop model and apply it to a real world example: observations of an x-ray bright point by TRACE and MDI. The x-ray bright point study employs detailed magnetic modeling, motivated by the 3D reconnection theory of Longcope (1998). Detailed comparison with observational data indicates that modeling within the constraints imposed by the reconnection theory cannot account for the extreme ultraviolet (EUV) emissions observed by TRACE.

II. LOOP MODEL

2.1 Equations and computational method

We solve the equations for mass (1), energy (2), and momentum (3) in a fully ionized hydrogen plasma confined to a flux tube of arbitrary shape.

$$\frac{\partial n_e}{\partial t} = -\frac{1}{A}\frac{\partial}{\partial x}\left(A n_e v\right). \tag{1}$$

$$\frac{\partial \varepsilon}{\partial t} = -\frac{1}{A}\frac{\partial}{\partial x}(A\varepsilon v) - \frac{P}{A}\frac{\partial}{\partial x}(Av) + \frac{1}{A}\frac{\partial}{\partial x}\left(A\kappa T^{5/2}\frac{\partial T}{\partial x}\right) - n_e^2\Lambda(T) + E_H. \tag{2}$$

$$\frac{\partial v}{\partial t} = \frac{-1}{n_e m_p}\frac{\partial P}{\partial x} + g_{\parallel} - v\frac{\partial v}{\partial x}. \tag{3}$$

In the above equations, n_e is the electron density, A is cross-sectional area, x is the coordinate along the loop, ε is internal energy, $P = (2/3)\varepsilon = 2n_e k_B T$ is pressure, and v is velocity. The state of the loop is fully specified by three variables: $n_e(x, t)$, $\varepsilon(x, t)$, $v(x, t)$.

The thermal conductivity is $\kappa \sim 10^{-6}$ in the corona (Spitzer 1962). For the transition region, κ includes not only thermal conduction, but heat flux due to particle diffusion region as described in Section 2.2 (Figure 2). The radiative loss function is plotted in Figure 1. The coronal portion of the radiative loss ($T > 10^5$ K) is derived from the calculations of Cook *et al.* (1989), substituting the Feldman (1992) coronal abundances (compare Martens, Kankelborg and Berger 1999). The transition region radiative losses ($T < 10^5$ K) are discussed in Section 2.2.

The 3D geometry of the loop enters the above equations in two ways: the cross-sectional area $A(x)$ and the acceleration of gravity along the loop $g_{\parallel}(x)$. We assume that $\beta \ll 1$ everywhere, so that A and $g_{\parallel}$ are not influenced by hydrodynamic forces.

The numerical model uses first-order spatial differencing on a staggered finite-volume grid. The spatial grid used for most of the examples in this paper has $N = 512$ elements, spaced in a nonuniform grid with $dx_i = (1 + \delta)\, dx_{i-1}$ for $i < 128$, and $dx_i = (1 + \delta)^{-1}\, dx_{i-1}$ for $i > 128$, $dx_0 = dx_N \sim 50$m, and $\delta \sim 0.1 \ll 1$. Derivatives for each time step dt are obtained from finite differences after a half-step $(1 + \eta)dt/2$, with the perturbation $\eta \sim 0.1$ added for stability. The Courant condition is used to derive a time interval Δt, which is in turn divided by a safety factor s to determine the step size: $dt = \Delta t/s$. The algorithm usually proves stable with $s = 2$; we typically use $s = 5$. Time step size dt is re-evaluated once per second of model time. Thermal conduction is handled implicitly.

Density and internal energy are defined inside each of N volume elements, and velocity is defined at the $N-1$ borders between volume elements. Upwind differencing is used on all advected quantities. The staggered grid allows evaluation of the differential quantities in equations (1-3) without interpolation on the grid, thereby minimizing diffusion in this first-order scheme. The first and last elements of the volume and velocity arrays are used for implementation of boundary conditions. Conservative forms are used for all advection terms to ensure that mass, energy and momentum are rigorously conserved. No effort has been made to provide a realistic treatment of shocks. As a result, there will usually be two grid points of intermediate pressure on a propagating shock front. Standing shocks are better represented.

In contrast to models previously described in the literature, the loop is allowed to be asymmetric. Boundary conditions are imposed only at the footpoints, where we impose a temperature of 10^4 K and no flow through the boundary.

The model incorporates a reservoir of chromospheric material at 10^4 K, using the method described by Klimchuk *et al.* (1987). Chromospheric condensation or evaporation adds or subtracts matter from this reservoir. In our implementation, the temperature of this chromospheric reservoir is maintained by arbitrarily setting the radiative loss function $\Lambda(T) = 0$ for $T < 10^4$ K. A difficulty with this arrangement is that the evaporation of large amounts of chromospheric material can cause the corona to extend into the most highly resolved portion of the grid, slowing execution of the code. Similarly, the condensation of a large amount of material can raise the level of the transition region to a point where the grid spacing is too coarse. We have therefore devised an algorithm, the *self-regulating chromosphere* (Appendix A), that gradually adds or subtracts mass at the base of the transition region (1.1×10^4 K). This optional feature uses feedback through a finely tuned control law to keep the transition region at a specified height.

2.2 Corrections for nonlocal effects in the lower transition region

Since the publication of the VAL transition region models, considerable progress has been achieved in modeling the lower transition region. The artificial "chromospheric plateau" at 2×10^4 K, introduced by VAL to account for the brightness of the hydrogen Lyman α line, has been replaced in the FAL models by real physics in the form of ambipolar diffusion. Ambipolar diffusion smooths the ionization gradient, with the dual effect of enhanced energy transport and enhanced radiative loss below 10^5 K.

Radiative loss. Although ambipolar diffusion and opacity are intrinsically nonlocal effects, we approximate their influence on energy balance by straightforward modification of the radiative and conductive loss terms in equation (2). That such an approximation is valid for the radiative losses is demonstrated by Avrett & Fontenla (198x) by comparing effective radiative loss for FAL models A, F, and C. We take $\Lambda(T)$ from FAL model C, which is close to the mean of the three FAL models. Among these three models, the maximum deviation from the mean in $\Lambda(T)$ is ± 33%. The resulting radiative loss is plotted in Figure 1. This result departs strongly from the radiative loss of McClymont & Canfield (1983) for the lower transition region (see the comparison by Avrett & Fontenla, 1991).

Heat flux. The heat flux F_H in the FAL model includes thermal conduction by electrons, atoms, and protons and also a large heat flux due to upward diffusion of neutral hydrogen and downward diffusion of protons (FAL Figure 3). If we assume that the ratio of F_H to the Spitzer conductivity ($\kappa \sim 10^{-6}$) depends only on the temperature, then an approximate correction to the thermal conductivity κ may be derived. The resulting effective value of κ is plotted in Figure 2.

We caution that these corrections are derived from steady state models. Their applicability to time dependent simulations must decrease as departures from a steady state temperature profile increase.

Ambipolar diffusion increases the efficiency of heat transport and radiation in the transition region. It also implies that the assumptions of the gasdynamic model hold at surprisingly low temperatures. In transition region models *without* particle diffusion, hydrogen is about 40% ionized at 10^4 K, and 65% ionized at $10^{4.2}$ K (Avrett and Fontenla 1991). However, ambipolar diffusion smooths the ionization gradient and lessens the concentration of neutral hydrogen at temperatures of $10^{3.9}$-$10^{4.3}$ K. With ambipolar diffusion, Avrett and Fontenla calculate 75% and 90% ionization at 10^4 K and $10^{4.2}$ K, respectively. As a result, a simple gasdynamic model assuming a fully ionized plasma can represent the base of the transition region with reasonable fidelity.

III. EXAMPLE: AN X-RAY BRIGHT POINT

3.1 Observations

On June 17, 1998, TRACE observed the quiet sun near disk center for 8 hours, 04:00 – 12:00 UT. Data was obtained in the 171 Å, 195 Å, and 1216 Å channels (the latter at half resolution), at a cadence of ~90s. The longest stretch of high quality data (with little or no radiation damage) is from 09:39 to 10:54 UT. Our analysis concerns a soft X-ray bright point (XBP) that was particularly prominent during that time. The bright point and its context among faint, quiet sun loops is pictured in Figure 3. These background loops give a rough indication of the background magnetic field in which the XBP is immersed. We have also a time series of four full-disk MDI magnetograms running from 08:00 – 17:49 UT. Figure 4 shows a portion of one MDI magnetogram, alongside a simultaneous TRACE 171 Å image. The bright point is clearly identified with a magnetic bipole.

The EUV data was reduced by first removing solar rotation, and then subtracting an interpolated background from a region of interest enclosing the XBP, using the algorithm described by Kankelborg *et al*. (1997). Movie 1 in the accompanying CD-ROM shows the evolution of the XBP at 1 arcsec resolution in 171 Å (Fe IX) and 195 Å (Fe XII), with solar rotation removed and background subtracted. The movie shows successive, multiple brightenings in each of several sub-loops within the XBP. Because of the continual movement and modulation in brightness of the sub-loops, it is difficult to ascertain whether a loop observed at a given time corresponds to another loop seen several minutes later. The reduced images were integrated over the entire XBP to obtain the light curves of Figure 5. Some key features of the light curves are:

- gradual brightening from 10:00 to 10:20 UT in 195 Å, and from 09:45 to 10:30 in 171 Å. Afterward, the brightness falls off somewhat more rapidly.
- The ratio of 171 Å to 195 Å signal varies from 1:1 to 2:1. Interestingly, on time scales shorter than ~600s, the variations in 171 Å and 195 Å are anticorrelated. This effect is most noticeable in the time period from 10:32 to 10:37 UT.
- Fluctuations of 10%–20% in brightness, on time scales of tens to hundreds of seconds.

We note that brightness fluctuations of order 10% are statistically significant and well measured, because the count rates (with exposures ~ 30s per EUV channel) in the background-subtracted images are always in excess of 10,000 detected photons per exposure.

3.2 Modeling

The XBP is clearly associated with the magnetic elements (poles) labeled P01 and N01 in Figure 4a. The complete sequence of MDI magnetograms reveals that separation between these poles, measured in the tangent plane, is approximately 11.3 Mm at 0936 UT, and decreases steadily at approximately 218 m/sec. At the same time each pole has a magnetic flux of approximately 1.1×10^{19} Mx, which decreases steadily at a rate of approximately $\dot{\Phi}_1 = 3.5 \times 10^{14}$ Mx/sec, presumably by subduction (see K. Harvey *et al*. in this volume). To investigate the effects of this convergence and cancellation upon the corona, we use a simplified model of the magnetic field. Point sources representing poles P01 and N01 steadily approach each other and their fluxes steadily decrease, while the “spectator poles” remain at positions and fluxes from the 0936 UT observation. A uniform horizontal background field, B_0 = 10 G directed 65˚ North of West, is added to reproduce the general context shown in the TRACE image.

This collection of poles and background field is used to model the magnetic field evolution in the vicinity of the P01/N01 bipole. The potential magnetic field reveals four categories of field lines in the bipole neighborhood (see figure 6). First there are "bipole field lines" which connect P01 to N01. Next, there are "monopole field lines" which either begin at P01 and leave the neighborhood, or enter the neighborhood to end at N01. Finally there are "background" field lines which enter and then leave the neighborhood without connecting to either P01 or N01. At the interface of all four domains lies a single magnetic field line: the *separator*. All bipole field lines must pass under the separator field line; the total flux in the bipole field will be denoted $\Phi_{P1\text{-}N1}$.

As the model magnetic field changes the amount of bipolar flux is found to decrease at $\dot{\Phi}_{P1\text{-}N1} \sim 1.9 \times 10^{14}$ Mx/sec; not as fast as the flux from each pole is being subducted. If we assume that only bipolar flux may be subducted (*i.e.* field lines with closely spaced footpoints), then new bipolar field lines must be "forged" at a rate of $\dot{\Phi}_1 - \dot{\Phi}_{P1\text{-}N1} = 1.6 \times 10^{14}$ Mx/sec in order to keep pace with subduction (see figure 7). New bipolar field lines are forged through the process of reconnection: two monopolar field lines, one beginning at P01 and the other ending at N01, are each broken in the middle, and "re-connected" into one bipolar field line and one background field line. This process of magnetic reconnection is believed to supply the energy which the observed XBP radiates and otherwise dissipates.

Faraday's law implies that the inferred rate of flux transfer, $\dot{\Phi} = 1.6 \times 10^{14}$ Mx /sec must accompany an electric field parallel to the magnetic separator. The total loop voltage, 1.6×10^{14} emu or 1.6 Megavolts, must appear in the corona (Longcope 1996). Over the 25 Mm long separator, this is an average electric field of 0.06 V/m, almost exactly equal to the Dreicer field.

It has been proposed (Longcope 1996, 1998) that field line reconnection occurs in sudden bursts, rather than through a smooth, steady transfer of flux. In other words, flux is transfered (reconnected) into the bipolar domain in bundles of size $\Delta\Phi$, at intervals of approximately $\tau = \Delta\Phi / \dot{\Phi}$. The reconnection of a single bundle occurs over a time presumably shorter than τ. Between these impulsive transfers, current I builds up along the separator, producing a compensating self-flux within the bipolar domain. The transfer of flux $\Delta\Phi$ across the current I does work on the plasma, equal to $\Delta E = I\,\Delta\Phi$ (if the current decreases during the transfer the energy released might be smaller by one half at the least). We propose to model the effect of this energy release on the plasma inside the flux tube $\Delta\Phi$.

The 171 Å image at 10:23:38 shows a single loop feature (see figure 8a) at the beginning of the most pronounced brightening phase. This loop is approximately 1.8

arcseconds across, implying a loop with minor radius 660 km. In the neighborhood of the separator, the model magnetic field has a strength of $B = 13$ G. If the observed loop has a similar field strength it contains $\Delta\Phi = 1.8 \times 10^{17}$ Mx. In our first model we take this EUV loop to be the result of a single impulsive transfer, simulate the resulting plasma evolution, and produce model light curves.

A field line immediately inside (beneath) the separator is identified as the axis of the loop. That portion of the field line within one Mm of the model's source plane, where point magnetic-charges are located, is removed (see figure 8c). The properties of the remaining 19 Mm field line portion are used to define the flux tube for the gas dynamic simulation described above, in particular its cross sectional area and the inclination of its axis. The simulation is first run to establish an equilibrium. A uniform volumetric heating of $q_0 = 7 \times 10^{-4}$ erg cm^{-3} s^{-1} (a total power input of 1.5×10^{22} erg/sec) is applied to yield a loop whose maximum temperature is $T_0 = 800{,}000$ K. This equilibrium state is intended to represent the pre-reconnection plasma, even though no single loop actually exists prior to reconnection.

At $t = 0$ the volumetric heating rate is increased to q_{rx}, for a duration t_{rx}, typically a few Alfvén loop-transit times, to model the energy deposition from fast reconnection. The heating rate is then returned to q_0 and the plasma is allowed to return to its previous equilibrium. The reconnection heating rate is set so that it generates energy ΔE over the time t_{rx}. The energy release ΔE is in turn set by the current I at the separator. We perform simulations using different values of the current, which we define to be $I = \theta\, I^*$, where $I^* = 8.8 \times 10^8$ emu (8.8×10^9 Amps) is a current characteristic of the separator (Longcope 1996). Thus the total liberated energy is taken to be

$$\Delta E = \theta\, I^*\, \Delta\Phi = \theta\; 1.6 \times 10^{26} \text{ ergs}.$$

where $\theta \leq 1$ is a free parameter of our model.

We have performed simulations at various values of the parameters t_{rx}, θ and T_0. The run with $\theta = 1.0$ ($\Delta E = 1.6 \times 10^{26}$ ergs), $T_0 = 800{,}000$ K and $t_{rx} = 10$ Alfvén transit times (145 seconds) shows typical behavior (movie 2). The loop temperature rises abruptly due to the increased heating, remains high (~ 3.5 MK) during the reconnection and then gradually returns to its initial value. The local plasma density and temperature can be used to calculate a theoretical response $S_\lambda(t)$ in each of the TRACE pass bands. The 171 Å and 195 Å curves, $S_{171}(t)$ and $S_{195}(t)$ shown in figure 9, become dark during the heating phase, as the loop's temperature is driven above the temperature range of both pass bands. As the loop cools through the temperature range of each filter there is a rise and then decay characteristic of the cooling time — 200 seconds.

Clearly the single 4 minute (250 second) brightening from the model light curve cannot represent the entire 45 minutes of elevated 171 Å and 195 Å emission observed. Actually, the movie shows that emission does comprise several different loops during this period. Theoretically we expect transfers of size $\Delta\Phi = 1.8 \times 10^{17}$ Mx to occur at intervals of $\tau = 1100$ seconds (19 minutes), so we might expect three or four such events to occur between 10:00 and 10:45. The resulting light curve would show each flux tube remaining bright for 250 seconds followed by 850 seconds of dim waiting. This cannot be construed to match the observed light curve. Our brief exploration of the model parameters θ, T_0 and t_{rx} has shown no exceptions; the principal difficulty stems from the short radiative cooling time, which does not change very much.

If we insist that magnetic reconnection, from the transfer of flux into the bipole P01/N01, is actually powering the observed XBP, then me must modify our model. At least two modifications seem possible. The brightening duration may be entirely dictated by the reconnection process, which far from *fast*, takes some 45 minutes (150 Alfvén times) to accomplish the flux transfer. This does not seem far-fetched in light of the many theoretical difficulties posed by fast reconnection. Unfortunately this logic implies that all details of the light curve reflect the reconnection process, which cannot be modeled at present. The subtly different alternative is the nanoflare hypothesis (Parker 1988): what appears to TRACE as a $\Delta\Phi = 1.8 \times 10^{17}$ Mx flux tube, actually consists of N smaller flux tubes of size $\delta\Phi = \Delta\Phi/N$. Each of these nano-tubes would brighten and dim independently, remaining visible for the same 250 second radiative cooling time. The interval between nano-brightenings, $\delta\Phi/\dot{\Phi}$, would be $1/N$ times shorter than the 1100 seconds between $\Delta\Phi$ transfers. If N were 6, for example, the repetition interval (180 sec) would be shorter than the cooling time, presumably resulting in a steadier brightening.

To demonstrate the nano-flare alternative we use the light curves $S_\lambda(t)$ from the $\theta = 1$, $t_{rx} = 145$ s run shown above. The reconnection model, the gasdynamic model and the integrated TRACE responses $S_\lambda(t)$ can all be scaled by the cross sectional area (i.e. by $\delta\Phi$). Thus the light curve from a nano-tube $\delta\Phi$ is simply $S_\lambda(t)/N$. We repeat copies of this scaled light curve at random intervals, chosen from a Poisson distribution whose mean is τ/N. We show the results of such a synthesis, with N=10, in figure (10). The pluses denote the locations of the individual impulses, although peak emission from a pulse occurs after a delay of approximately 6 minutes, as shown in fig. 9. Reducing both the amplitude of the pulse-response and the mean waiting time between pulses preserves the mean count rate per channel

$$\bar{S}_\lambda \equiv \frac{1}{\tau} \int S_\lambda(t) dt .$$

The run shown in fig. 9 was found to have the highest mean count rates of all that were tried; $\bar{S}_{171} = 184$ DN/sec and $\bar{S}_{195} = 92$ DN/sec. These values are about four times less than the observed count rates. It seems doubtful that the TRACE calibration (Handy *et al.* 1999) could be that far off. Moreover, the anticorrelation evident between the TRACE 171 Å and 195 Å channels on time scales shorter than ~600 s did not occur in any of our models; rather, the theoretically predicted light curves always showed a positive correlation.

IV. CONCLUSIONS

Self-consistent forward modeling of the coupled system of corona, transition region and magnetic field makes it possible to connect theory to observation in new ways. Toward this end, we have developed a gasdynamic loop model with arbitrary 3D flux tube geometry. Our model is the first to incorporate recent advances in the related fields of transition region modeling and coronal abundances.

As a first application of the loop model, we constructed a detailed 3D picture of an X-ray bright point, incorporating a separator flux tube model constrained by observations of the photospheric magnetic field and of EUV emissions. The separator model harmonizes well with the morphology of the observed bright point. The gasdynamic loop model with energetic inputs derived from the minimum current corona theory of Longcope (1996) was used to synthesize EUV light curves. The synthetic light curves fell short of the observed EUV luminosity in both TRACE bands. We tried unsuccessfully to reconcile this discrepancy by changing the time profile of the energy release: adjusting the reconnection time and dividing each reconnection event into N "nanoflares". At best, the predicted emissions were about half of the observed emissions. It seems that the MCC reconnection model by itself is not sufficient to explain the observations. The observations also show a puzzling anticorrelation between the 171 Å and 195 Å channels, something that our models failed to anticipate. If these conclusions can be confirmed and extended to more X-ray bright points, it will present a serious challenge to the "minimum current" picture of coronal magnetic fields.

Acknowledgements

This work was supported by NASA grant NAG5-7877

Appendix A. Active maintenance of chromospheric depth

Our model uses a nonuniform grid of fixed dimensions to ensure that the steep temperature gradients of the transition region are well-resolved, without having an excessive number of grid points in the corona. The transition region floats atop an artificial 10^4 K chromosphere, and therefore assumes a natural profile that is not influenced by the boundary conditions at the footpoint. While this arrangement is robust under small evaporations or condensations of chromospheric material, a large change in the volume of the chromosphere can lead to an undersampled transition region or an oversampled corona. In the worst case, the chromosphere may evaporate entirely, pressing the transition region against the footpoint boundary and artificially steepening the temperature gradient. The latter problem may be alleviated by adding extra grid points at the base, extending the reservoir of chromospheric material as described in Section 3.1. A more sophisticated numerical approach might add an adaptive mesh to maintain optimal sampling of the transition region and corona.

We have instead developed a simple strategy to solve these problems. Our code includes an optional feature that automatically adds or subtracts chromospheric material as needed. This self-regulating chromosphere attempts to maintain a specified depth $d = d_0$, where d is defined as position above the footpoint of the 1.1×10^4 K isotherm. The overriding concerns in developing this strategy were stability and the minimization of dynamical effects:

- To avoid large phase delays in the feedback between addition or subtraction of chromospheric mass and the resulting change in d, mass is added or subtracted by changing the density ($n_e \rightarrow n_e + dn_e$) at the $T = 1.1 \times 10^4$ K isotherm. The control law governing this mass adjustment may be expressed as $dn_e = f(\Delta)$, where f is an odd function of the dimensionless displacement $\Delta \equiv (d - d_0)/d_0$.
- In order to avoid pressure fluctuations that would propagate as waves, the density correction dn_e is applied with no corresponding adjustment of the internal energy. As a result, addition (subtraction) of chromospheric material leads to a slight temperature decrease (increase), which directly pushes the $T = 1.1 \times 10^4$ K isotherm upward (downward), leading to an immediate adjustment in Δ.
- To suppress instabilities and oscillations, the response of the control law for small Δ is cubic rather than linear: $dn_e \propto \Delta^3$, $\Delta < 1$.
- The applied correction is scaled to be a small fraction of the smallest density in the chromosphere: $dn_e << n_{e,\min}$. This ensures that density changes will be small, and also prevents density from running away due to positive feedback.

Our resulting control law always adopts the smallest of two possible adjustments:

$$dn_e = \frac{1}{2s} n_{e,\min} \min\left[\Delta^3,\ 1\right], \qquad \text{(A1)}$$

where s is the safety factor that stabilizes the timestepping scheme (Section 2.1).

References

Avrett, E. H.: 1991, in 'Mechanisms of Chromospheric and Coronal Heating', P. Ulmschneider, E. R. Priest, and R. Rosner (eds.), Springer-Verlag.

Avrett, E. H. and Fontenla, J. M.: 1991, in 'Mechanisms of Chromospheric and Coronal Heating', P. Ulmschneider, E. R. Priest, and R. Rosner (eds.), Springer-Verlag.

Cook, J. W., Cheng, C.-C., Jacobs, V. L. and Antiochos, S. K.: 1989, *Astrophys. J.* **338**, 1176

Feldman, U.: 1992, *Physica Scripta* **46**, 202.

Fontenla, J. M., Avrett, E. H., and Loeser, R.: 1990, *Astrophys. J.* **355**, 700.

Gabriel, A. H.: 1976, *Phil. Trans. R. Soc. London A* **281**, 339.

Kankelborg, C. C., Walker, II, A. B. C. and Hoover, R. B.: 1997, *Astrophys. J.* **491**, 952.

Klimchuk, J. A., Antiochos, S. K., and Mariska, J. T.: 1987, *Astrophys. J.* **320**, 409.

Longcope, D. W.: 1998, *Astrophys. J.* **507**, 433

Longcope, D. W.: 1996, *Sol. Phys.* **169**, 91.

Martens, P. C. H., Kankelborg, C. C., and Berger, T. E.: 1999, *Astrophys. J.* submitted.

McClymont, A. N. and Canfield, R. C.: 1983, *Astrophys. J.* **355**, 700.

Parker, E. N.: 1988, *Astrophys. J.* **330**, 474,

Peres., G., Rosner, R., Serio, S., and Vaiana, G. S.: 1982, *Astrophys. J.* **252**, 791.

Rosner, R., Tucker, W. H., and Vaiana, G. S.: 1978, *Astrophys. J.* **220**, 643.

Rabin, D.: 1991, *Astrophys. J.* **383**, 407.

Spitzer, L.: 1962, 'Physics of Fully Ionized Gases', Wiley-Interscience, New York.

Vernazza, J. E., Avrett, E. H., and Loeser, R.: 1981, *Astrophys. J. Suppl.* **45**, 635.

Vesecky, J. F., Antiochos, S. K. and Underwood, J. H.: 1979, *Astrophys. J.* **233**, 987.

Figure Captions

Figure 1. An improved radiative loss model for solar coronal loop plasmas. Ambipolar diffusion (Avrett 1991) raises the temperature of the H Lyman α peak. Coronal losses are greatly enhanced by the FIP effect (Martens, Kankelborg and Berger 1999).

Figure 2. An improved model of heat flux in the lower transition region, based on the FAL results. Diffusion of protons and neutral hydrogen results in enhancements of up to two orders of magnitude over the Spitzer conductivity.

Figure 3. A deep exposure shows faint overlying loops near the XBP (circled in green). Apparent direction of the background field is indicated by the blue line.

Figure 4. (a) MDI magnetogram. (b) TRACE 171 Å image. The XBP corresponds closely to the N01–P01 bipole.

Figure 5. EUV light curves for the XBP.

Figure 6. Representative field lines from the neighborhood of bipole P01/N01. Bipole field lines are shown in red, monopole field lines in green, and the separator field line in blue.

Figure 7. The evolution of fluxes during the convergence of bipole P01/N01. (a) The total flux in poles Φ_1, and the bipolar flux $\Phi_{P1\text{-}N1}$. (b) The decreasing monopole flux implies a rate of magnetic reconnection.

Figure 8. The model flux tube. (a) TRACE 171 Å image from which flux $\Delta\Phi$ is calculated. (b) The model flux tube viewed with same projection. Green circles show the boundaries of the finite volume elements, which are concentrated toward the end of the tube. (c) A different view of the model flux tube.

Figure 9. (a) Maximum temperature during the simulation. The 145 s period of heating is indicated by a horizontal bar. (b) Integrated response $S_\lambda(t)$ (DN/sec) for each TRACE pass band from simulation of reconnection event.

Figure 10. Synthesized light curve from nano-flares of $\delta\Phi = 1.8 \times 10^{16}$ Mx, being transfered at an average rate of once every 110 seconds (i.e. $N = 10$). The instant of each nanoflare is shown by a plus. Mean count rates calculated from $S_\lambda(t)$ are indicated by horizontal lines.

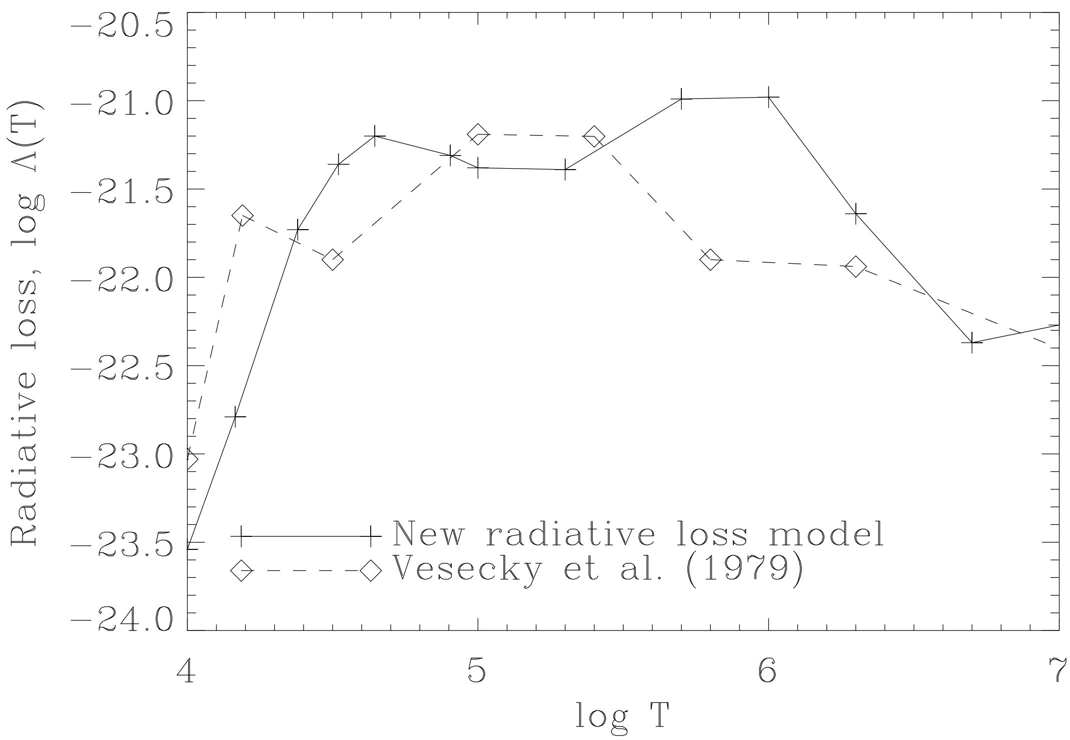

Fig. 1. An improved radiative loss model for solar coronal loop plasmas. Ambipolar diffusion (Avrett 1991) raises the temperature of the H Lyman α peak. Coronal losses are greatly enhanced by the FIP effect (Martens, Kankelborg and Berger 1999).

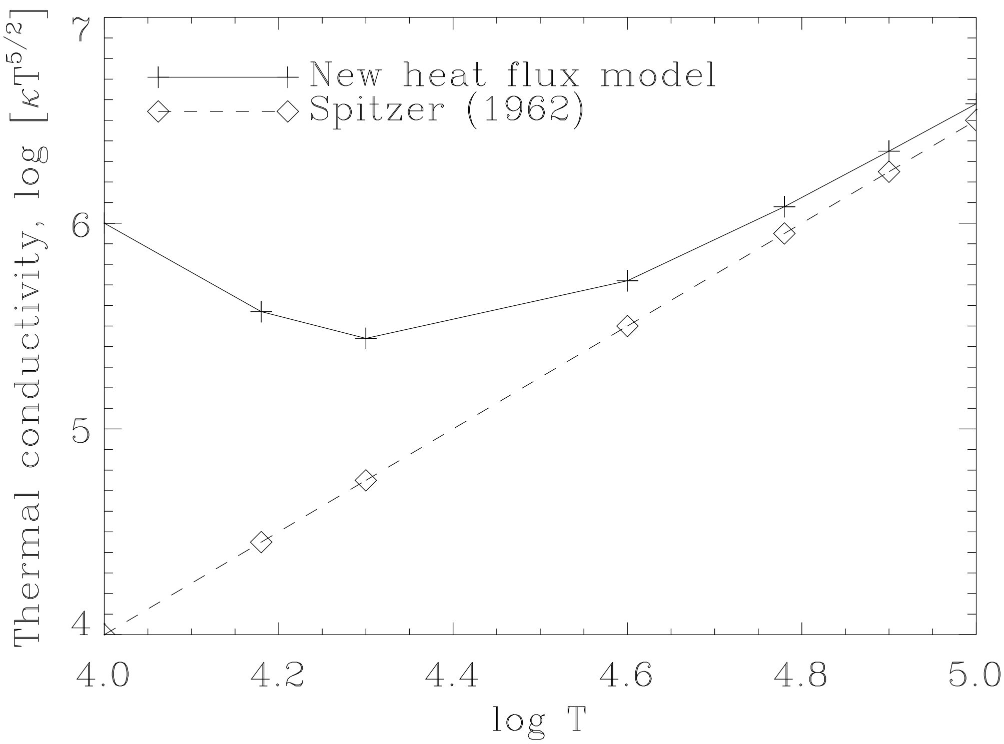

Fig. 2. An improved model of heat flux in the lower transition region, based on the FAL results. Diffusion of protons and neutral hydrogen results in enhancements of up to two orders of magnitude over the Spitzer conductivity.

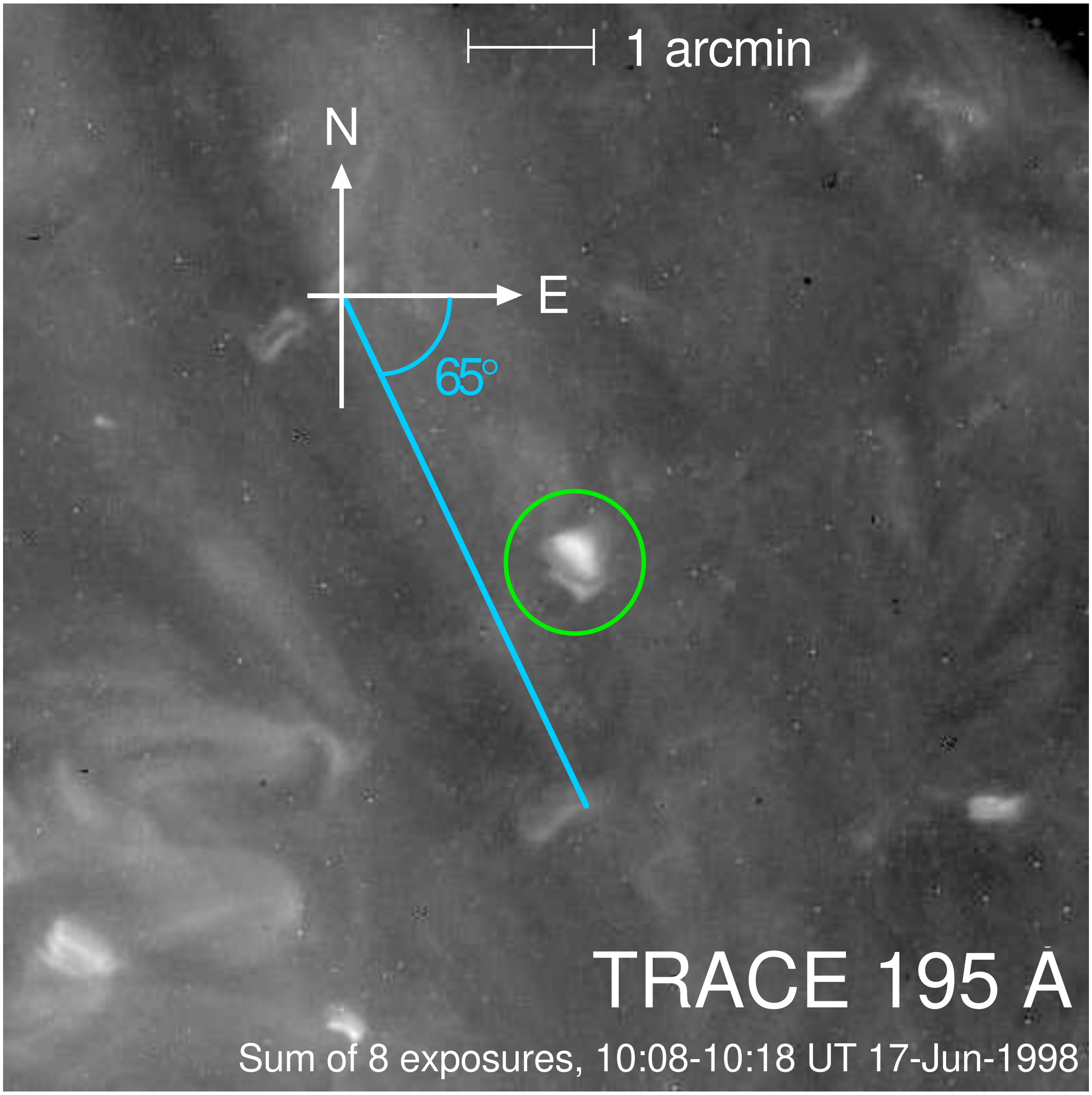

Fig. 3. A deep exposure shows faint overlying loops near the XBP (circled in green). Apparent direction of the background field is indicated by the blue line.

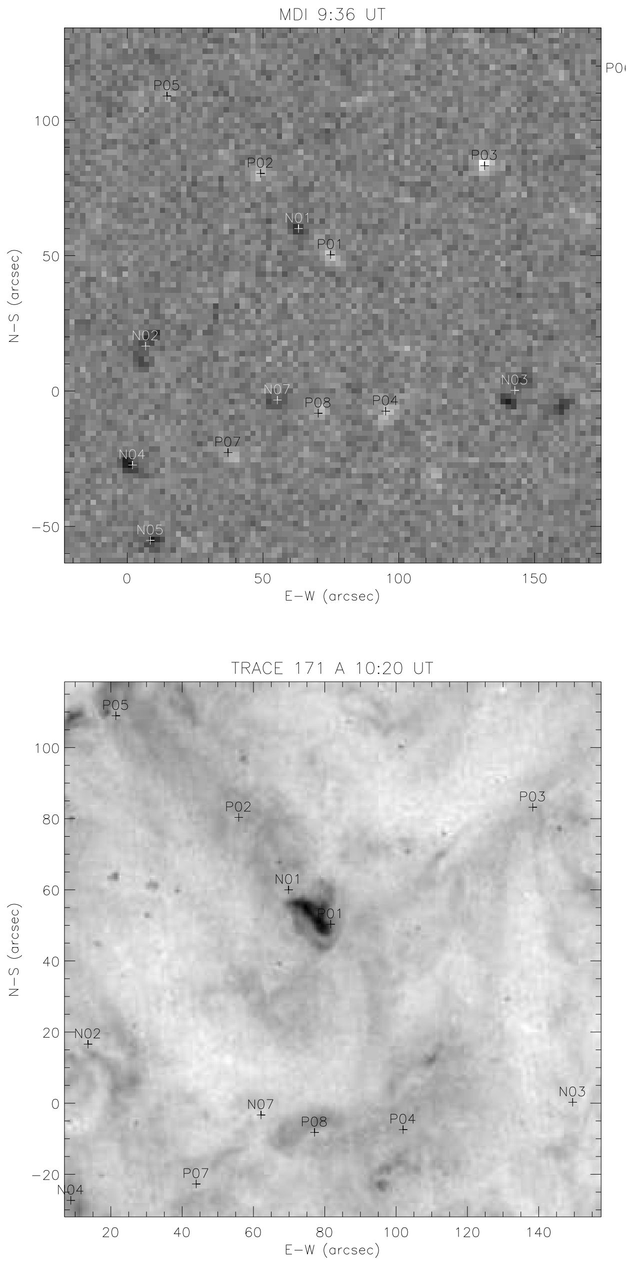

(a)

(b)

Fig. 4. (a) MDI magnetogram. (b) TRACE 171 Å image. The XBP corresponds closely to the N01–P01 bipole.

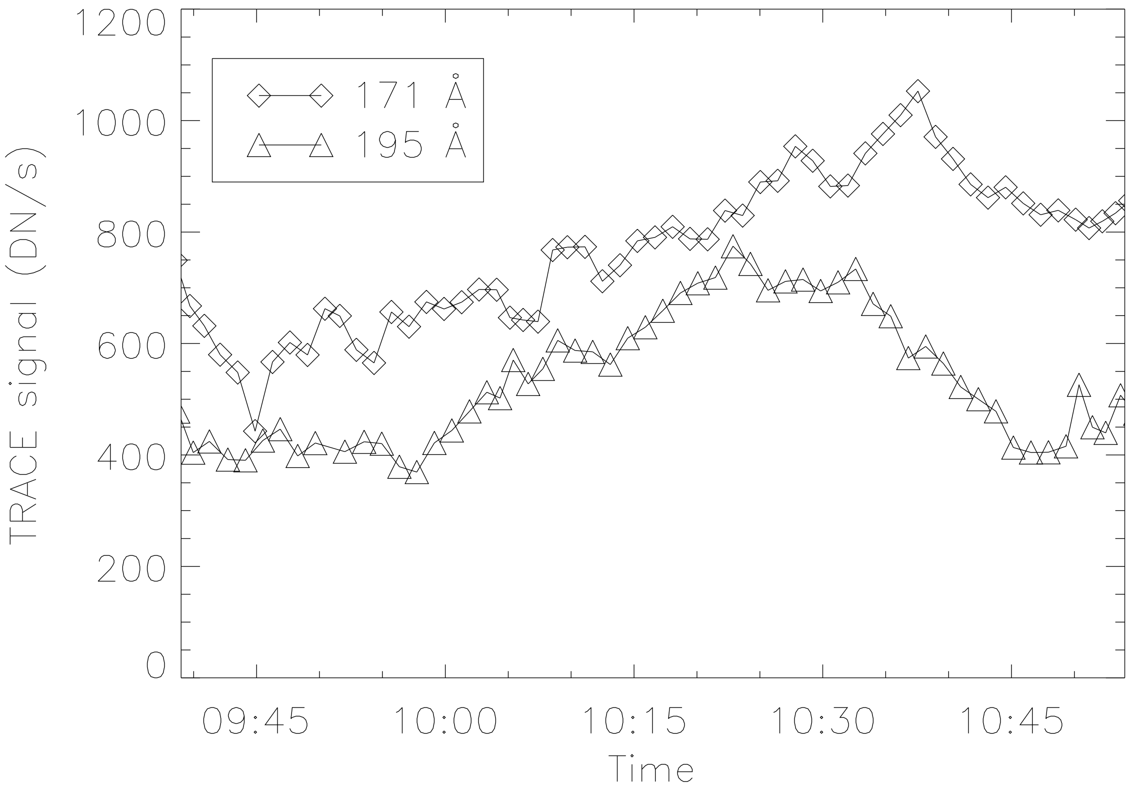

Fig. 5. EUV light curves for the XBP.

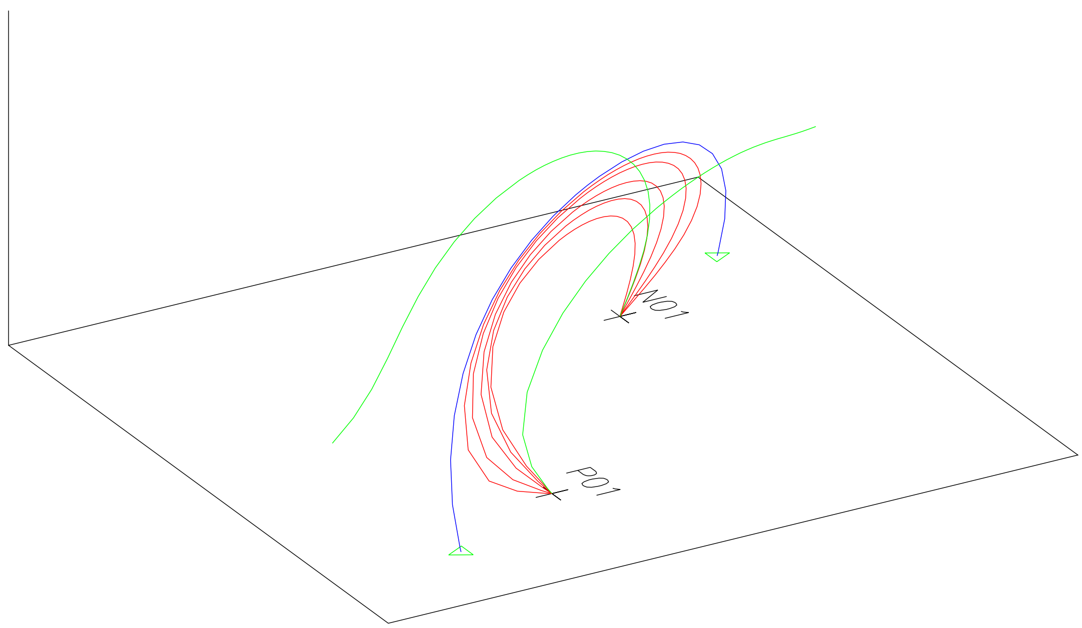

Fig. 6. Representative field lines from the neighborhood of bipole P01/N01. Bipole field lines are shown in red, monopole field lines in green, and the separator field line in blue.

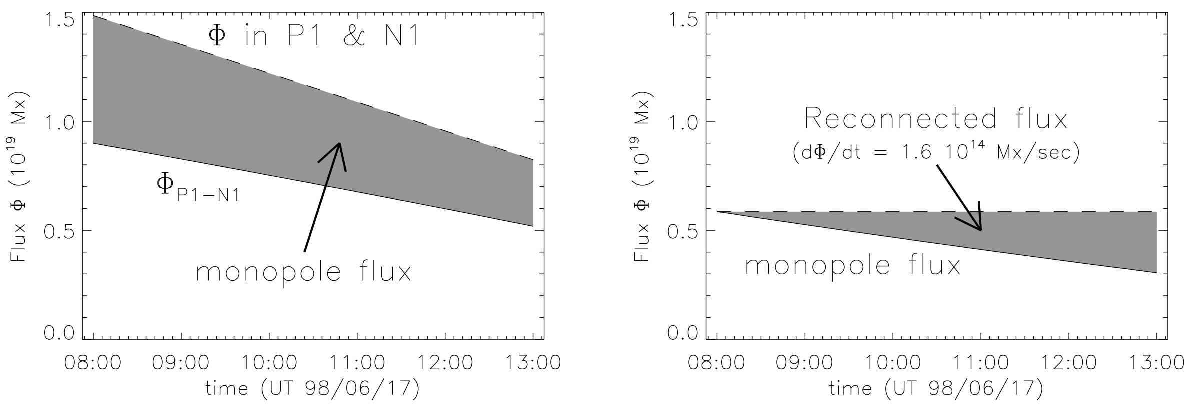

Fig. 7. The evolution of fluxes during the convergence of bipole P01/N01. (a) The total flux in poles Φ_1, and the bipolar flux $\Phi_{P1\text{-}N1}$. (b) The decreasing monopole flux implies a rate of magnetic reconnection.

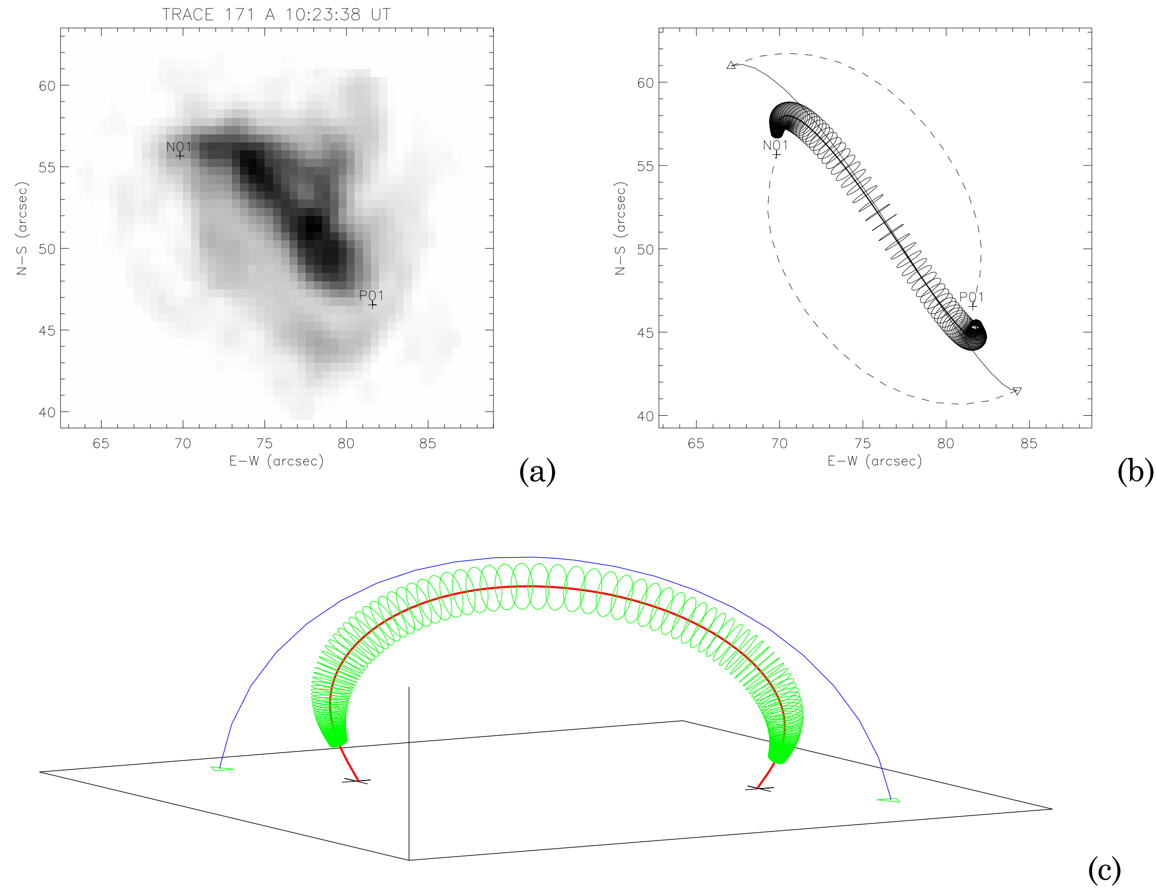

Fig. 8. The model flux tube. (a) TRACE 171 Å image from which flux $\Delta\Phi$ is calculated. (b) The model flux tube viewed with same projection. Green circles show the boundaries of the finite volume elements, which are concentrated toward the end of the tube. (c) A different view of the model flux tube.

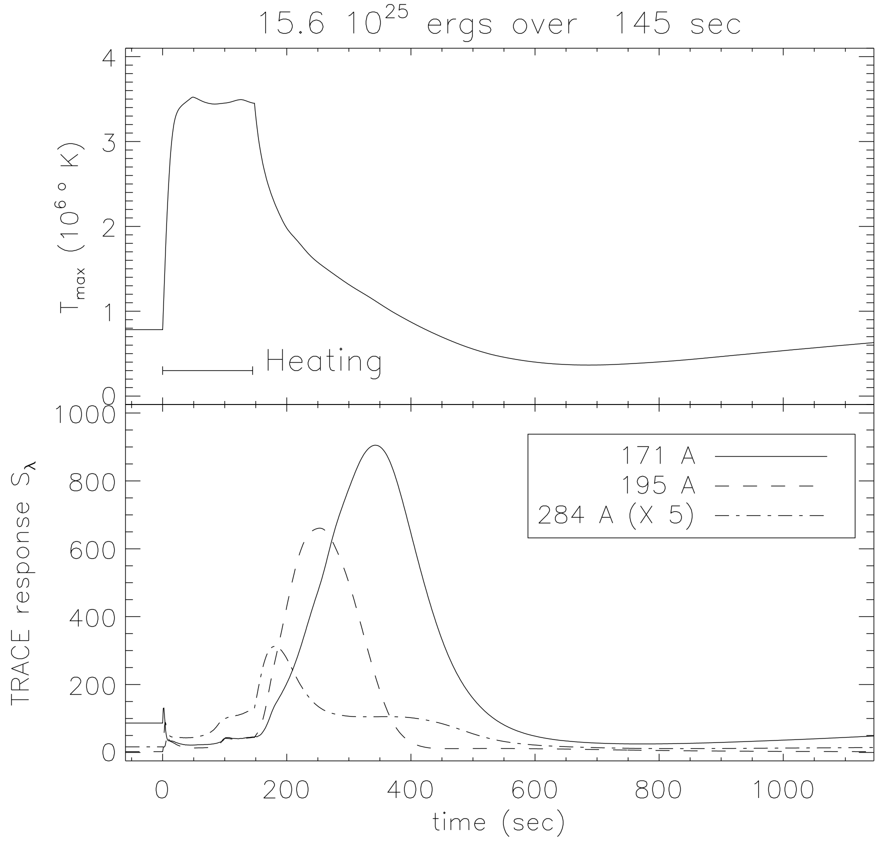

Fig. 9. (a) Maximum temperature during the simulation. The 145 s period of heating is indicated by a horizontal bar. (b) Integrated response $S_\lambda(t)$ (DN/sec) for each TRACE pass band from simulation of reconnection event.

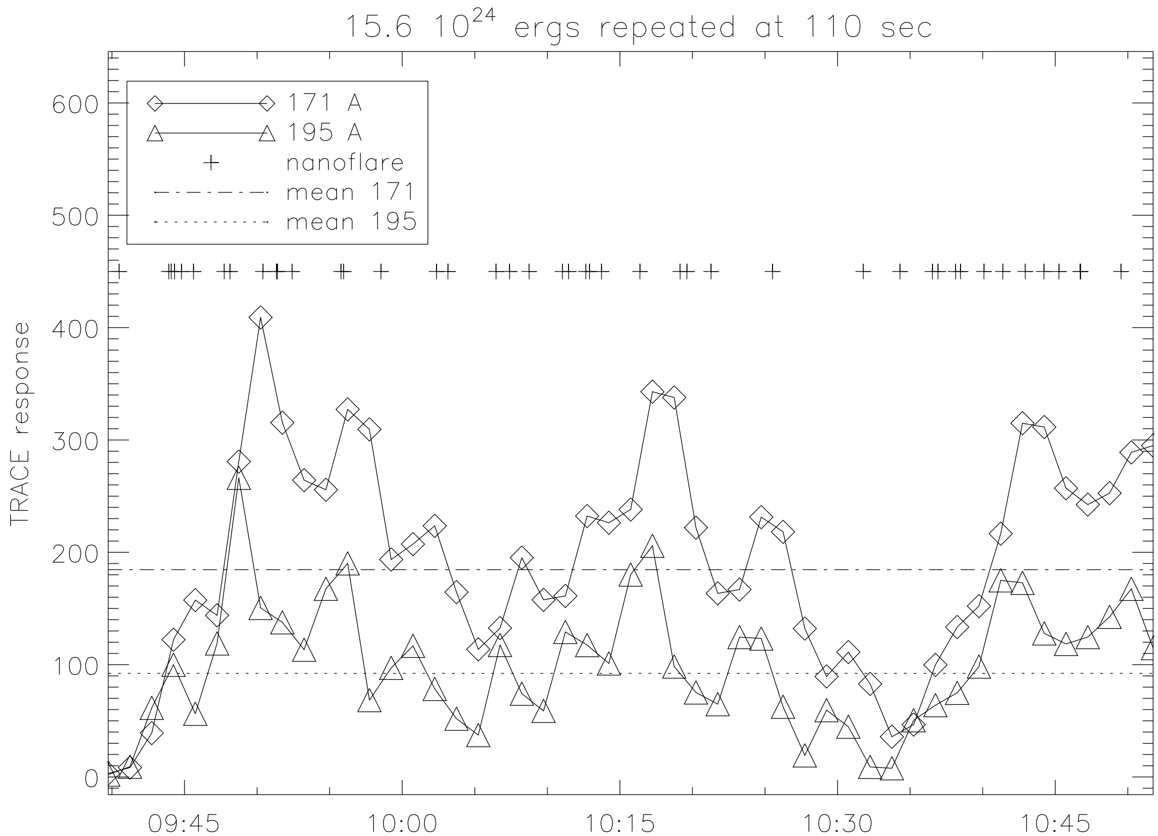

Fig. 10. Synthesized light curve from nano-flares of $\delta\Phi = 1.8 \times 10^{16}$ Mx, being transfered at an average rate of once every 110 seconds (i.e. $N = 10$). The instant of each nanoflare is shown by a plus. Mean count rates calculated from $S_\lambda(t)$ are indicated by horizontal lines.